European Congress on Computational Methods
in Applied Sciences and Engineering (ECCOMAS 2012)
J. Eberhardsteiner et.al. (eds.)
Vienna, Austria, September 10-14, 2012

A PHASE-FIELD TOPOLOGY OPTIMIZATION MODEL USING A DOUBLE-OBSTACLE FUNCTION

Tomohiro Takaki

Mechanical and System Engineering, Graduate School of Science and Technology,
Kyoto Institute of Technology,
Matsugasaki, Sakyo, Kyoto 606-85858, Japan
e-mail: takaki@kit.ac.jp

Keywords: topology optimization, phase-field method, double-obstacle function, stiffness maximization

Abstract. *A phase-field topology optimization model, which maximizes the structure stiffness under fixed material volume using a double-obstacle function, has been developed. By using the double-obstacle function, the interface region can be defined clearly. By performing two-dimensional simulations for a cantilever model and comparing the results to those obtained from the phase-field topology model with a double-well function, the fundamental characteristics of the developed model have been investigated. As a result, although some unstable structures were observed, almost all results coincided with those obtained by a phase-field topology model with a double-well function.*

1 INTRODUCTION

Topology optimization that optimizes material layout, which includes changes in the number and shape of holes within a given design space, is a method having the highest degree of freedom among optimization design methods [1]. The level-set method is the method most often used to track surface position in topology optimization simulations. Although the phase-field method is another surface tracking method and is the most powerful numerical method used in material microstructure design, there are only a few topology optimization models in which the phase-field method is used as the surface tracking method instead of the level-set method [2]. In our previous study, we have developed a phase-field topology optimization model that maximizes structure stiffness [3]. This model was derived using the same procedure as in a material microstructure model and the coefficients used in the phase-field equation were clearly related to the surface energy and surface thickness.

In the present study, we have developed a phase-field topology optimization model using a double-obstacle function instead of the double-well function used in ordinary phase-field models [2, 3]. By performing two-dimensional simulations for a cantilever model and comparing the results to those obtained using the phase-field topology model with a double-well function, the fundamental characteristics of the developed model have been confirmed. The double-obstacle function is employed in the multiphase-field model [4], for which application to multicomponent structure design is anticipated.

2 PHASE-FIELD TOPOLOGY OPTIMIZATION MODEL

In this chapter, by following previous work [3], a phase-field topology optimization model with a double-obstacle function is derived together with a model with a double-well function. Hereafter, the phase-field topology optimization models with double-well and double-obstacle functions are referred to as "Model I" and "Model II," respectively.

The phase-field variable ϕ is defined as ϕ = 1 in solid and ϕ = 0 in vapor (or hole) and changes smoothly and rapidly at the surface region. The free energy functional that maximizes the structure stiffness under a constant volume can be described as

$$F = F_m + F_p - F_f, \tag{1}$$

where F_m is the free energy in bulk, F_p is the penalty energy to keep a constant volume, and F_f is the external force potential. These are expressed as

$$F_m = \int_V f dV = \int_V \left(f_{grad} + f_{doub} - f_{elast} \right) dV, \tag{2}$$

$$F_p = k \left| V - V_0 \right|, \tag{3}$$

$$F_f = - \int_S u_i \bar{p}_i dS. \tag{4}$$

In Eq. (2), the gradient energy density f_{grad}, the double-well potential f_{doub}, and the elastic strain energy f_{elast} are described as follows:

$$f_{grad} = \frac{a^2}{2} \left| \nabla \phi \right|^2, \tag{5}$$

$$f_{doub} = W q \left(\phi \right), \tag{6}$$

$$f_{elast} = \frac{1}{2} C_{ijkl} \left(\phi \right) \varepsilon_{ij} \varepsilon_{kl} = \frac{1}{2} C_{ijkl} \varepsilon_{ij} \varepsilon_{kl} \rho \left(\phi \right). \tag{7}$$

Here, a is the gradient coefficient, W is the energy barrier, ε_{ij} is the strain tensor, and C_{ijkl} is the elastic coefficient tensor. $q(\phi)$ is the double-well or double-obstacle function and $\rho(\phi)$ is the solid density function. For $q(\phi)$ and $\rho(\phi)$, we chose the following two types of function:

Model I:

$$q(\phi) = \phi^2 (1-\phi)^2, \tag{8}$$

$$\rho(\phi) = \phi^3 \left(10 - 15\phi + 6\phi^2\right); \tag{9}$$

Model Ⅱ:

$$q(\phi) = \phi(1-\phi), \tag{10}$$

$$\rho(\phi) = \frac{8}{\pi}\left\{\frac{1}{4}(2\phi-1)\sqrt{\phi(1-\phi)} + \frac{1}{8}\arcsin(2\phi-1)\right\} + \frac{1}{2}. \tag{11}$$

Figure 1 shows the profiles of $q(\phi)$ and $\rho(\phi)$ for Model I (solid line) and Model Ⅱ (broken line). For $q(\phi)$, Eq. (8) and Eq. (10) are multiplied by 16 and 4, respectively, to set those maximum values to one.

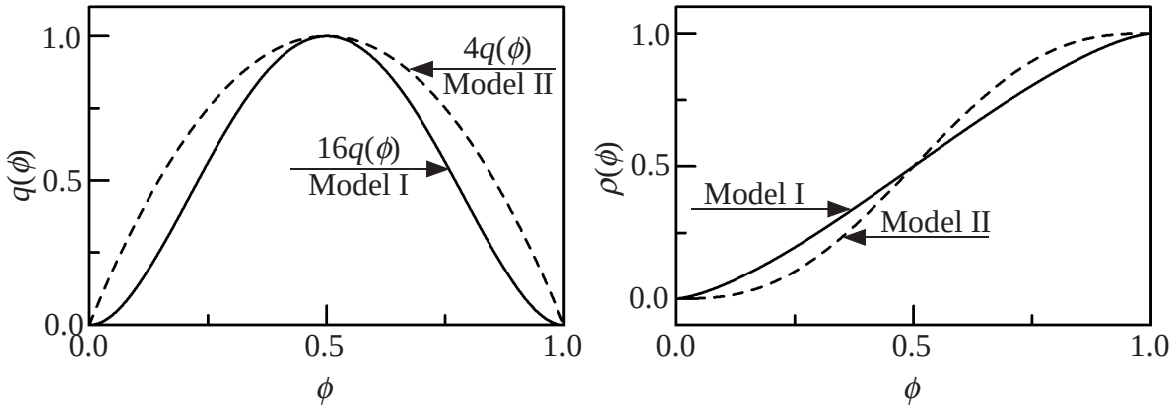

Figure 1: Profiles of $q(\phi)$ and $\rho(\phi)$.

In Eq. (3), k is the penalty coefficient, V_0 is the prescribed constant volume, and V is the current volume defined as

$$V = \int_V \rho(\phi)\, dV. \tag{12}$$

In Eq. (4), u_i is the displacement vector and $\bar{p}_i$ is the prescribed surface pressure vector.

By following the Allen–Cahn equation, the evolution of the phase-field variable ϕ can be derived as the following equation:

$$\frac{\partial \phi}{\partial t} = -M_\phi \frac{\delta F}{\delta \phi} = -M_\phi \left(\frac{\delta F_m}{\delta \phi} + \frac{\delta F_p}{\delta \phi} - \frac{\delta F_f}{\delta \phi}\right), \tag{13}$$

where M_ϕ is the phase-field mobility. By substituting Eq. (1) into Eq. (13), the following time evolution equations for both models can be obtained:

Model I:

$$\frac{\partial \phi}{\partial t} = M_\phi \left[a^2 \nabla^2 \phi + 4W\phi(1-\phi)\left(\phi - \frac{1}{2} + \frac{15}{2W}\frac{1}{2} C_{ijkl}\varepsilon_{ij}\varepsilon_{kl}\phi(1-\phi) \pm \frac{15}{2W} k\phi(1-\phi)\right)\right]; \tag{14}$$

Model Ⅱ:

$$\frac{\partial \phi}{\partial t} = M_\phi \left[a^2 \nabla^2 \phi + 2W \left\{ \phi - \frac{1}{2} + \frac{1}{2W} \frac{1}{2} C_{ijkl} \varepsilon_{ij} \varepsilon_{kl} \cdot \frac{8}{\pi} \sqrt{\phi (1-\phi)} \pm \frac{1}{2W} k \frac{8}{\pi} \sqrt{\phi (1-\phi)} \right\} \right]. \tag{15}$$

By making the time of Eqs. (14) and (15) dimensionless and substituting the relations between a and W and the interface energy γ and interface thickness δ (with b a constant related to δ), or

Model Ⅰ:

$$a = \sqrt{\frac{3\delta\gamma}{b}}, \quad W = \frac{6\gamma b}{\delta}; \tag{16}$$

Model Ⅱ:

$$a = \frac{2}{\pi}\sqrt{2\delta\gamma}, \quad W = \frac{4\gamma}{\delta}, \tag{17}$$

into Eqs. (14) and (15), the following final time evolution equations for ϕ can be derived:

Model Ⅰ:

$$\frac{\partial \phi}{\partial t} = \frac{\delta^2}{8b^2} \nabla^2 \phi + \phi (1-\phi) \left(\phi - \frac{1}{2} + \beta \right); \tag{18}$$

Model Ⅱ:

$$\frac{\partial \phi}{\partial t} = \frac{\delta^2}{\pi^2} \nabla^2 \phi + \left(\phi - \frac{1}{2} + \beta \right). \tag{19}$$

Here, β is set as

Model Ⅰ:

$$\beta = \begin{cases} \frac{e(\phi)}{e_{ave}} \beta_1 + 4\alpha\beta_2 \phi (1-\phi) & \cdots \quad e(\phi) < e_{ave}, \\ \beta_1 + 4\alpha\beta_2 \phi (1-\phi) & \cdots \quad e(\phi) \geq e_{ave}; \end{cases} \tag{20}$$

Model Ⅱ:

$$\beta = \begin{cases} \frac{e(\phi)}{e_{ave}} \beta_1 + 2\alpha\beta_2 \sqrt{\phi (1-\phi)} & \cdots \quad e(\phi) < e_{ave}, \\ \beta_1 + 2\alpha\beta_2 \sqrt{\phi (1-\phi)} & \cdots \quad e(\phi) \geq e_{ave}, \end{cases} \tag{21}$$

where β_1 and β_2 are the constants satisfying $\beta_1 + \beta_2 = 0.5$, and $e(\phi)$ is the elastic strain energy at the surface region expressed as

Model Ⅰ:

$$e(\phi) = \frac{1}{2} C_{ijkl} \varepsilon_{ij} \varepsilon_{kl} \phi (1-\phi); \tag{22}$$

Model Ⅱ:

$$e(\phi) = \frac{1}{2} C_{ijkl} \varepsilon_{ij} \varepsilon_{kl} \sqrt{\phi (1-\phi)}, \tag{23}$$

with e_{ave} the average value of $e(\phi)$. The coefficient α in Eqs. (20) and (21) is used to satisfy the constant volume with high accuracy and is determined by $\alpha = (V_1^n - V_0)/(V_1^n - V_2^n)$, where $V_1^n = \int_V \rho(\phi_1^n)\, dV$ is the volume calculated under α = 0 and $V_2^n = \int_V \rho(\phi_2^n)\, dV$ is the volume calculated under α = 1. As shown here, the evolution equations for ϕ, Eqs. (18) and (19), are solved three times at every time step.

The stress field is calculated by solving the principle of virtual work $\int_V \delta\varepsilon_{ij}\sigma_{ij} dV = \int_S \delta u_i p_i dS$, the strain-displacement relations $\varepsilon_{ij} = (u_{i,j} + u_{j,i})/2$, and the stress–strain relations $\sigma_{ij} = C_{ijkl}\varepsilon_{ij}$ by using a finite element method with four-node elements in a plane strain problem, where u_i is the displacement, p_i is the external pressure, ε_{ij} is the strain, σ_{ij} is the stress, C_{ijkl} is the elastic coefficient, and δ means the virtual quantities.

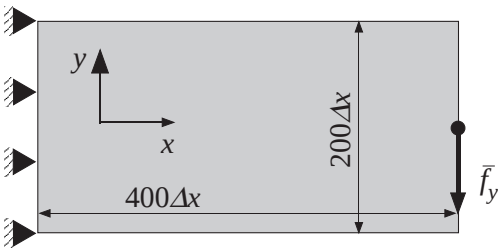

Figure 2: Cantilever model.

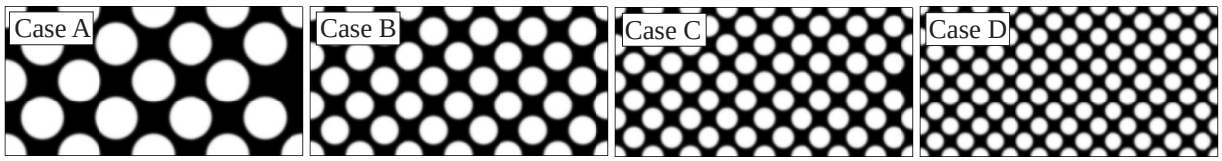

Figure 3: Initial conditions.

3 NUMERICAL CONDITIONS

Stiffness maximization simulations of a cantilever using the two developed models are performed and the results are compared. Figure 2 shows the employed cantilever model with size $400\Delta x \times 200\Delta x$, where Δx is the square element size. The nodal displacements of the left side are constrained in all directions and an external force is applied to the central node on the right side.

Figure 3 shows four initial conditions, where the black region indicates the solid and the white region indicates the holes. The volume fraction of the solid is set to be 50%. The phase-field profiles shown in Fig. 3 are set by using the following equilibrium profiles:

Model I:

$$\phi_{eq} = \frac{1}{2}\left\{1 - \tanh\left(\frac{b}{\delta}r\right)\right\}; \tag{24}$$

Model II:

$$\phi_{eq} = \frac{1}{2}\left\{1 - \sin\left(\frac{\pi}{\delta}r\right)\right\}. \tag{25}$$

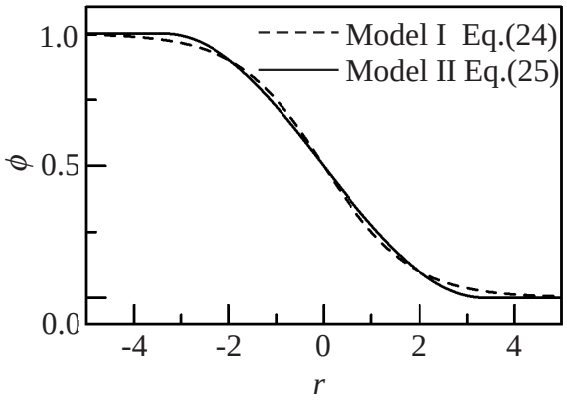

Figure 4: Equilibrium phase-field profiles for Model I and Model II.

Figure 4 shows the phase-field profiles around the interface indicated by Eqs. (24) and (25). Here, $\delta_{\mathrm{II}} = c\delta_{\mathrm{I}} = 1.682\delta_{\mathrm{I}}$, δ_{I} = 4, and b = 2.2 are employed, where δ_{I} and δ_{II} are the interface thickness δ for Model I and Model II, respectively. The relation $c = 1.682$ is derived by setting $a_{\mathrm{I}} = a_{\mathrm{II}}$ or $M_{\phi\mathrm{I}} = M_{\phi\mathrm{II}}$.

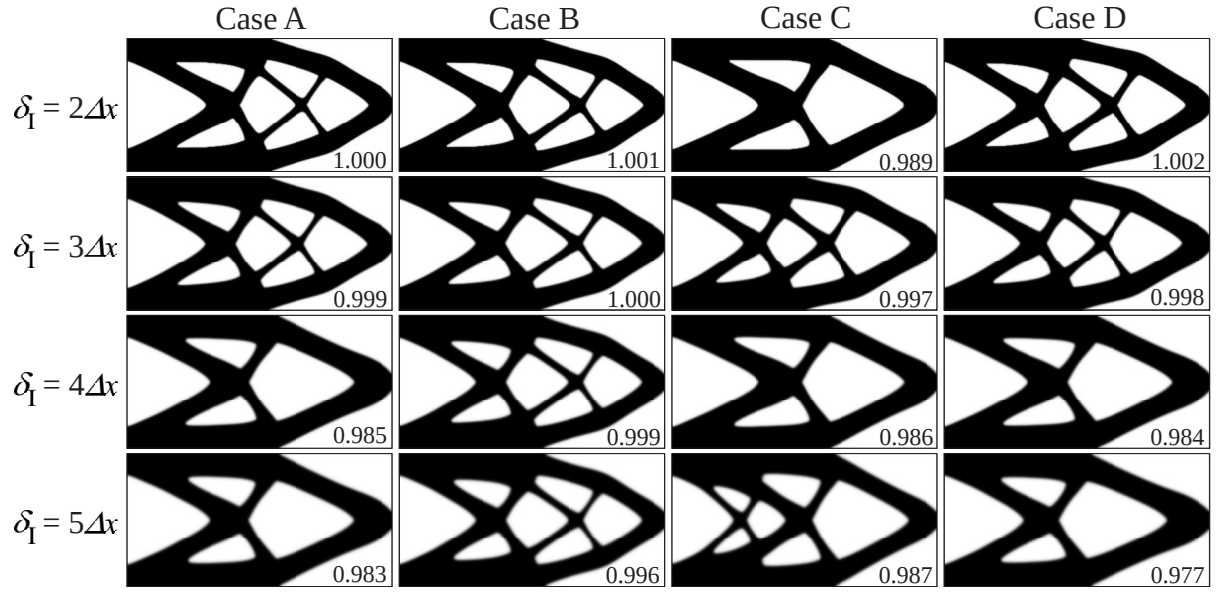

(a) Model I

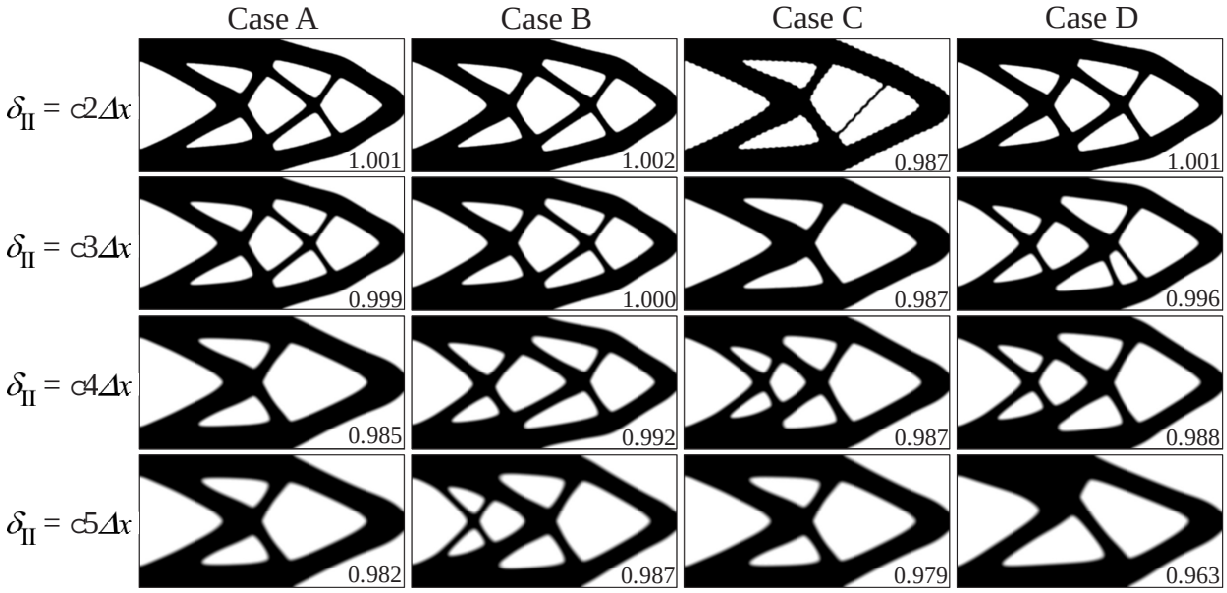

(b) Model II

Figure 5: Final morphologies.

4 NUMERICAL RESULTS

Figure 5 shows the final morphologies at 10000 steps for (a) Model I and (b) Model II. Here, the time increment Δt is set to $8b^2(\Delta x)^2/(5\delta^2)$ and $\pi^2(\Delta x)^2/(5\delta^2)$ for Models I and II, respectively. The interface thicknesses δ_{I} for Model I are $2\Delta x$, $3\Delta x$, $4\Delta x$, and $5\Delta x$, and δ_{II}

values for Model Ⅱ are $3.364\Delta x$, $5.046\Delta x$, $6.728\Delta x$, and $8.410\Delta x$ in order to keep the relation $\delta_{\mathrm{II}} = 1.682\delta_{\mathrm{I}}$. The numerical values indicated in Fig. 5 are the stiffness ratios for the condition $\delta_{\mathrm{I}} = 2\Delta x$ and Case A.

In Fig. 5, the effects of initial morphology on the final morphology are not absent but are relatively small. There are one or two types of topologies with the same interface thickness, although there are a few exceptions. Therefore, it is concluded that the dependencies on the initial morphology are relatively small. For the effects of interface thickness on the final morphology, it is observed that the stiffness increases with decreasing interface thickness. However, if the interface thickness become smaller than $2\Delta x$, the calculation become unstable. Therefore, the suitable interface thickness is $\delta = 2\Delta x$ or $3\Delta x$.

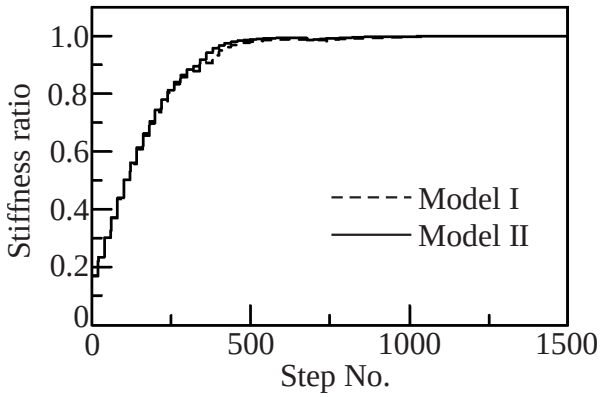

Figure 6: Variations in stiffness ratio for the condition of $\delta = 2\Delta x$ and Case A.

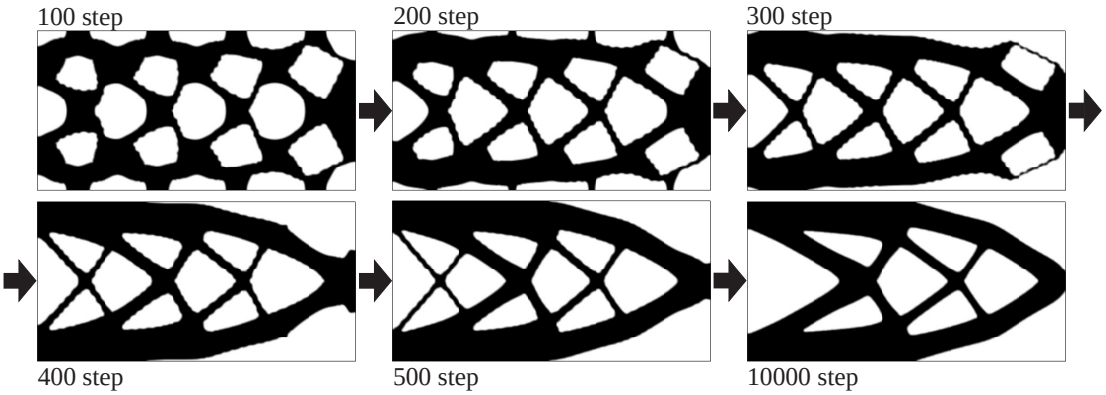

Figure 7: Morphological changes for Model I, with $\delta = 2\Delta x$, for Case A.

Comparing Model I and Model Ⅱ, we can see similar final morphologies. Figure 6 shows variations in the stiffness ratio for the condition of $\delta = 2\Delta x$ and Case A. The stiffness is defined as the value where the applied force $\bar{f}$ is divided by the displacement of the point. The ordinate of Fig. 6 is the ratio to the initial condition. It is confirmed that variations in the stiffness ratio for both models are almost identical with monotonic increases. Figure 7 shows the variations of morphology of Model I for the conditions of Fig. 6. At the beginning of the calculation, the circular holes changed shape to squares in order to arrange the solid along the principal stress direction. After that, the solid in the upper and lower regions around the applied concentrated

force disappears. These morphological changes occur to increase the structure stiffness, as seen in Fig. 6. However, from Fig. 5(b), a few nonsymmetrical morphologies in the upper and lower regions can be observed in Model II. Therefore, it is concluded that a phase-field topology optimization model with a double-obstacle function can be used to calculate almost the same final morphologies as a model with a double-well function, although it sometimes exhibits unstable results.

5 CONCLUSIONS

A phase-field topology optimization model with a double-obstacle function was derived together with a model with a double-well function. By performing two-dimensional topology optimization simulations for a cantilever subjected to a concentrated force, the fundamental characteristics of the developed model were investigated. As a result, it was commonly concluded for both models that the effects of initial morphology on the final morphology are relatively small and higher stiffness values are obtained for thinner interfaces. Furthermore, the developed model with a double-obstacle function can be used to calculate an almost similar final morphology with a similar stiffness as a model with a double-well function, although some final nonsymmetrical shapes appear in upper and lower regions of the model with a double-obstacle function.

REFERENCES

[1] M. P. Bendsœ, O. Sigmund: Topology Optimization (2002), Springer.

[2] A. Takezawa, S. Nishiwaki, M. Kitamura: Shape and topology optimization based on the phase field method and sensitivity analysis. *Journal of Computational Physics*, 229 (2010), 2697–2718.

[3] T. Takaki: Development of phase-field topology optimization model and its fundamental performance evaluations. *Transactions of the Japan Society of Mechanical Engineers Series A*, 77 (2011), 1840–1850 (in Japanese).

[4] I. Steinbach, F. Pezzolla: A generalized field method for multiphase transformations using interface fields. *Physica D*, 134 (1999), 385–393.